Korean J. Chem. Eng., **31**(1), 132-141 (2014)
DOI: 10.1007/s11814-013-0201-x

pISSN: 0256-1115
eISSN: 1975-7220

Effect of bed void volume on pressure vacuum swing adsorption for air separation

Yo Han Kim*, Dong Geun Lee*, Dong Kyu Moon*, Sang-Hoon Byeon, Hyung Woong Ahn***, and Chang Ha Lee*,†**

*Department of Chemical and Biomolecular Engineering, Yonsei University, Seoul 120-749, Korea
**Department of Environmental Health, Korea University, Seoul 136-701, Korea
***Institute for Materials and Processes, University of Edinburgh, UK
(*Received 10 June 2013 • accepted 4 October 2013*)

Abstract−The effects of a poorly packed bed on the pressure vacuum swing adsorption (PVSA) process were investigated experimentally and theoretically by a five-step two-bed PVSA system. At first, the adsorption dynamics of a zeolite LiX bed for air separation (78 mol% N_2, 21 mol% O_2 and 1 mol% Ar) was studied at various adsorption pressures and flow rates. In breakthrough results, the effect of adsorption pressure on variations in bed temperature was greater than that of the feed flow rate. A combined roll-up of Ar and O_2 by N_2 propagation was observed and the roll-up plateau reached about 4 mol%. The fluid dynamic behavior of the poorly packed bed was simulated at each step in the PVSA process. The pressure and velocity profiles in the non-isobaric steps were clearly different from those of a normally packed bed. The two-bed PVSA process using one poorly packed bed with additional 1% void volume in feed end of bed could produce a purity of 92.3 mol% O_2 from air, which was almost 1% purity lower than the PVSA with normal two beds. Even small asymmetry between beds, due to poor bed packing, could greatly reduce the product purity in the PVSA process.

Keywords: Air Separation, Pressure Vacuum Swing Adsorption, Zeolite LiX, Poorly Packed Bed

INTRODUCTION

Applications of enriched oxygen include enhanced combustion in glass furnaces, electric arc furnaces, oxygen bleaching in pulp and paper industries, the cement industry, wastewater treatment, fish farming, environmental remediation, glass-blowing, oxygen bar, the medical field and hydrogen production from methanol reformation in fuel cells [1-3]. Even though there is an increasing demand for O_2 with more than 95 or 99% purity [4,5], it is not always necessary to produce extremely high purity oxygen since many industrial applications still only require oxygen-enriched air [6].

Classical cryogenic distillation has been widely recognized as one of the most common methods for oxygen production from air. Cryogenic processes for oxygen production are highly efficient and are quite common, but this technology is not compatible with relatively small oxygen plants [7].

The pressure swing adsorption (PSA) process has become a widely used unit operation for gas separation or purification [8,9]. One of the uses for the PSA process is nitrogen or oxygen production from air [10]. For nitrogen production, a carbon molecular sieve (CMS) is generally used, which is kinetically selective for oxygen. For oxygen production from air, it is preferable to use a nitrogen selective adsorbent. The adsorption materials used in oxygen production for PSA include a variety of zeolites, such as 4A, 5A, 10X, 13X, LiX, LiLSX, and LiAgX, which selectively adsorb nitrogen from a nitrogen/oxygen mixture gas while allowing oxygen molecules to pass through the unit [11-14]. The primary reason for this is the interaction between the quadrupole moment of N_2 and the cation of the zeolite framework. The various PSA processes that generate O_2 from ambient air using zeolites have been widely studied [15-21]. In addition, the application of zeolite LiX to PSA has been expanded to various industrial fields because the lithium cation, with its high polarizing power, provides strong interactions with N_2 [22].

In addition, a consistent packing quality for each bed is one of the more important factors in multi-bed PSA operation. It is expected that the fluid dynamics of an unbalanced bed, which has a greater void volume at specific sections of the bed by poor packing, differs from normal beds. Nevertheless, only a limited number of computational fluid dynamics (CFD) studies related to fixed bed adsorption have been completed in spite of its potential applicability [23-26]. Some CFD studies have been reported in a fixed-bed reactor and annular packed beds, and fluid flow distribution and heat transfer have been investigated in detail [27,28].

The adsorption dynamics of zeolite LiX bed for air separation (N_2 : O_2 : Ar=78 : 21 : 1 mol%) was studied at various adsorption pressures and flow rates. The poorly packed parts in the bed generally happen during an initial period of packing stage. Moreover, in the PSA operation, the adsorption step is typically changed to produce high purity product before the mass transfer zones of impurities are reached at the product end. In the study, the fluid dynamics (pressure and velocity profiles) of an unbalanced bed, which was poorly packed with adsorbents at the feed end, was studied by a CFD simulation at each step in the pressure-vacuum swing adsorption (PVSA) process. The result of the five-step two-bed PVSA process with an unbalanced bed was compared experimentally and theoretically with that of the normal PVSA process. The validity of the simulation, a non-isothermal and non-adiabatic dynamic model incorporating mass and energy balances, the linear driving force (LDF) model, and the loading ratio correlation (LRC) isotherm model, was confirmed by a comparison of the experimental breakthrough results.

†To whom correspondence should be addressed.
E-mail: leech@yonsei.ac.kr

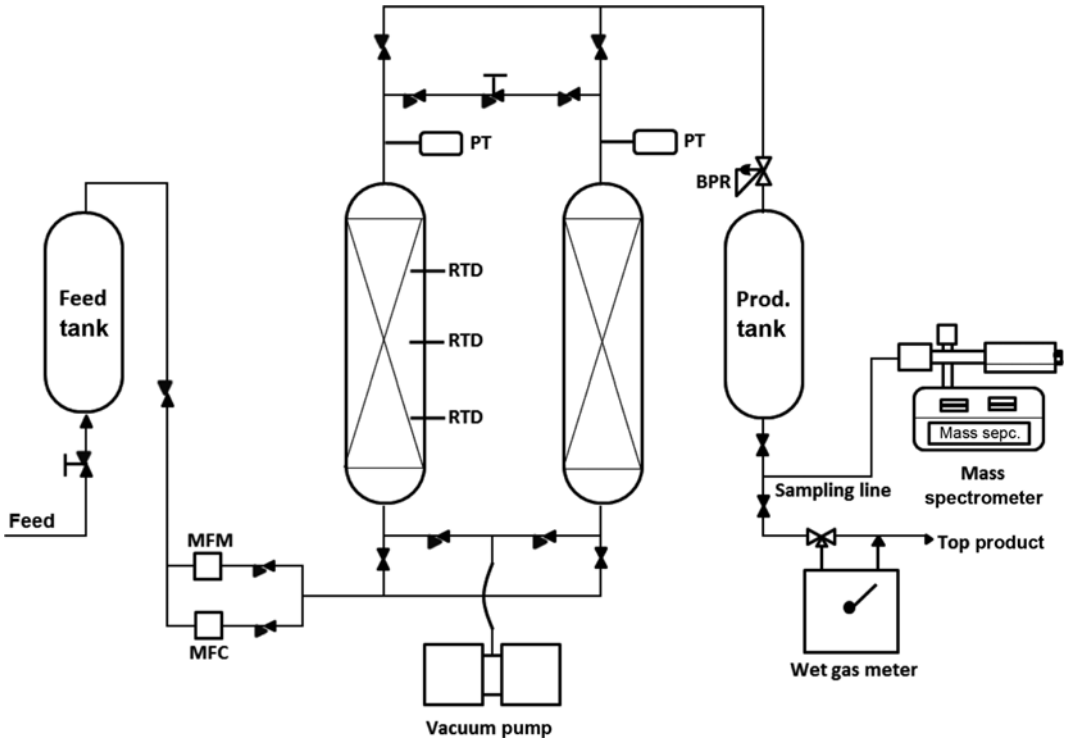

Fig. 1. Schematic diagram of the apparatus for a two-bed PVSA process.
MFC : mass flow controller MFM : mass flow meter PT : pressure transducer BPR : back pressure regulator
RTD : resistance temperature detector

EXPERIMENTAL SECTION

A schematic of the experimental apparatus for the PVSA process is shown in Fig. 1. The adsorption bed was 100 cm long with a 3.5 cm inner diameter. The zeolite LiX (UOP Co., WE-J750) was activated at 523 K for more than 12 h. To prevent contamination by fine particles, glass wool and wire mesh were installed at both the inlet and outlet parts of the bed. Three RTDs (Pt 100 Ω) were installed at a position of 0.1, 0.5 and 0.8 m from the feed inlet and two pressure transducers were located at each end of the bed. A silica trap bed of 50 cm in length was installed ahead of the feed tank for complete dehydration of the feed.

A flow line consisting of 1/4 inch stainless steel tube and solenoid valves was located in a position appropriate for controlling the gas flow at each step. The pre-calibrated mass flow controller (Bronkhorst High-tech, F-201C, Netherlands) was installed between the feed tank and the adsorption bed to control the feed flow rate. To maintain bed pressure, a back pressure regulator was located at the product end. The effluent gas was analyzed by a quadrupole mass spectrometer (QMG 422, Balzers, Germany). Since the system was fully computerized, the solenoid valves were controlled by a computer and all data such as concentration, temperature, pressure and flow rate were automatically saved during the experiment.

The commercial dry air consisted of 78 mol% N_2, 21 mol% O_2 and 1 mol% Ar, and was used as a feed gas. Breakthrough experiments were conducted in the range of 1.3 to 4.3 atm adsorption pressure and 2 to 6 LPM feed flow rate. The bed was saturated with oxygen as an initial condition.

Recent PVSA process for air separation is generally operated at lower than 2 atm adsorption pressure and shorter than 30 sec cyclic time due to compression energy and productivity [29]. In the previous studies, three-bed PVSA process using two zeolite 10X beds and one CMS bed was reported to produce high purity oxygen from air [3,11]. The process was operated at 1.5-3 atm adsorption pressure and 0.3-0.55 vacuum pressure and could overcome the limited oxygen purity of conventional zeolite PVSA.

In this study, since PVSA process using zeolite LiX can show high performance in air separation, PVSA process was operated at a similar condition to the PVSA using zeolite 10X. As an example

Table 1. Characteristics of adsorbent and adsorption bed

Adsorbent	Zeolite LiX
Type	Sphere
Pellet density, ρ_p [kg/m^3]	1.2
Particle porosity, α [-]	0.34
Bed density, ρ_B [kg/m^3]	620
Average particle diameter [m]	1.7E-3
Adsorption bed	
Length, L [m]	1
Inside radius, R_{Bi} [m]	17.5E-3
Outside radius, R_{Bo} [m]	19.25E-3
Heat capacity of column, C_{pw} [kJ/kg·K]	0.502
Density of column, ρ_w [kg/m^3]	7830
Internal heat transfer coefficient, H_{in} [kJ/m^2·K·sec]	38.49E-3
External heat transfer coefficient, H_{out} [kJ/m^2·K·sec]	14.23E-3

Table 2. Operating conditions for breakthrough experiments

	Feed	Adsorption pressure [atm]	Feed flow rate [LSTP/min]	Remark
Break 1.		1.3	4	
Break 2.			2	
Break 3.	Ternary	2.3	4	Base experiment
Break 4.	(N_2 : O_2 : Ar=79 : 20 : 1 vol%)		6	
Break 5.		3.3	4	
Break 6.		4.3	4	

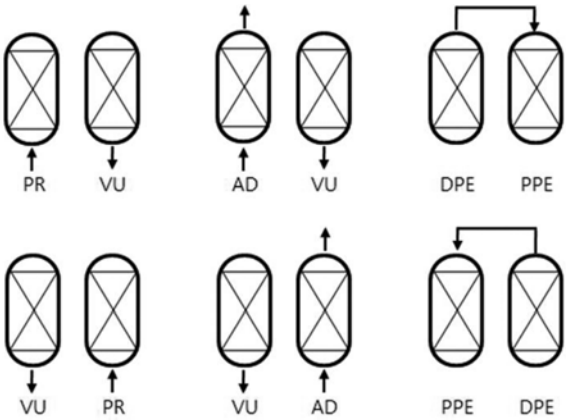

Process

BED I	PR ↑	AD ↑	DPE ↑	VU ↓		PPE ↓
BED II	VU ↓		PPE ↓	PR ↑	AD ↑	DPE ↑
Time[s]	70		25	40	30	25

Fig. 2. Cyclic sequence and step for the two-bed PVSA.
PR : pressurization AD : adsorption
VU : vacuum DPE : depressuring pressure equalization
PPE : pressuring pressure equalization

run, PVSA process using zeolite LiX was operated at 2.3 atm adsorption pressure and 0.38 atm vacuum pressure. For the PVSA process with one poorly packed bed, the additional 1% void volume was made by adding 1/8 inch pipe pieces in the section from the feed inlet to 10 cm of the bed. More detailed characteristics of the adsorbent and bed including heat transfer coefficients are shown in Table 1. Each experimental condition is listed in Table 2.

A typical five-step cyclic sequence was applied to the two-bed PVSA process: (1) pressurization with the feed gas (PR), (2) high-pressure adsorption (AD), (3) depressurizing pressure equalization (DPE), (4) vacuum desorption (VU), and (5) pressurizing pressure equalization (PPE). The cyclic sequence and a simple flow diagram are illustrated in Fig. 2.

MATHEMATICAL MODEL

To understand the dynamic behavior of the adsorption bed, a set of mathematical models was developed. A complete non-isothermal dynamic model in this study was considered with the following assumptions [11-13,30]: (1) the gas phase behaves as an ideal gas mixture, (2) radial concentration and temperature gradients are negligible, (3) thermal equilibrium between adsorbents and bulk flow is assumed, (4) the flow pattern is described by an axially dispersed plug flow model, (5) axial conduction in the wall can be neglected, and (6) the pressure drop along the bed is considered using Ergun's equation [14-17]. The material balance of each component for the bulk phase in the adsorption column is given by

$$\frac{\partial y_i}{\partial t}+\frac{RT}{P}\rho_s\left(\frac{1-\varepsilon}{\varepsilon}\right)\frac{\partial q_i}{\partial t}+\frac{\partial(uy_i)}{\partial z}-D\frac{\partial^2 y_i}{\partial z^2}=0 \tag{1}$$

and the overall mass balance can be written as

$$\frac{RT}{P}\rho_s\left(\frac{1-\varepsilon}{\varepsilon}\right)\sum_{i=1}^{n}\frac{\partial q_i}{\partial t}+\frac{\partial u}{\partial z}=0 \tag{2}$$

where D_L is axial dispersion coefficient. In this model the effects of all mechanisms which contribute to axial mixing are lumped into a single effective axial dispersion coefficient. More detailed models, which include, for example, radial gradient, are generally not necessary. And in many cases it is in fact possible to neglect axial dispersion and assume ideal plug flow. However, when mass transfer resistance at the external film and/or within adsorbent pellet is prominent at low feed rate, the weight of axial dispersion term increases, making this term important.

If ideal gas law applies to these equations, these equations can be transformed into:

$$-D_L\frac{\partial^2 y_i}{\partial z^2}+\frac{\partial y_i}{\partial t}+u\frac{\partial y_i}{\partial z}+\frac{RT}{P}\frac{1-\varepsilon}{\varepsilon}\rho_p\left(\frac{\partial \overline{q}_i}{\partial t}-y_i\sum_{j=1}^{n}\frac{\partial \overline{q}_j}{\partial t}\right)=0 \tag{3}$$

and the overall mass balance can be represented as follows:

$$-D_L\frac{\partial^2 P}{\partial z^2}+\frac{\partial P}{\partial t}+P\frac{\partial u}{\partial z}+u\frac{\partial P}{\partial z}-PT\left(-D_L\frac{\partial^2}{\partial z^2}\left(\frac{1}{T}\right)+\frac{\partial}{\partial t}\left(\frac{1}{T}\right)+u\frac{\partial}{\partial z}\left(\frac{1}{T}\right)\right)+\frac{1-\varepsilon}{\varepsilon}\rho_p RT\sum_{j=1}^{n}\frac{\partial \overline{q}_j}{\partial t}=0 \tag{4}$$

These equations are somewhat complicated to solve analytically and the difficulty becomes worse when energy balance is also considered. Therefore, another simplified approach to the mass balance equation has been made using the so-called equilibrium theory to understand adsorption dynamics. If axial dispersion and pressure drop through the column are neglected and velocity variation due to adsorption or desorption is also neglected, Eq. (1) can be reduced to:

$$\frac{\partial c_i}{\partial z}+u\frac{\partial c_i}{\partial t}+\frac{1-\varepsilon}{\varepsilon}\rho_p\frac{\partial \overline{q}_j}{\partial t}=0 \tag{5}$$

Assuming thermal equilibrium between the fluid and particles, the energy balance for the gas and solid phases is given by

$$(\varepsilon\rho_g C_{pg}+(1-\varepsilon)\rho_s C_{ps})\frac{\partial T}{\partial t}=-\varepsilon\rho_g C_{pg}\frac{\partial(uT)}{\partial z}+\varepsilon K_z\frac{\partial^2 T}{\partial z^2}$$
$$+(1-\varepsilon)\rho_s\sum_{i=1}^{n}\left(\Delta H_{ads,i}\frac{\partial q_i}{\partial t}\right)-\varepsilon\frac{2h_{in}}{R_{in}}(T-T_w) \quad (6)$$

Here, the axial dispersion, D_z, and effective axial thermal conductivity, K_z, can be calculated by empirical correlations, which were discussed in detail in the previous study [31]. And, practically, these two coefficients contributed to simulation convergence.

The commercial scale process for air separation is nearly adiabatic and feed-end temperature is affected by temperature variation in a pretreatment layer for H_2O and CO_2 [32,33]. However, since the diameter of the bed used was small, heat loss through the wall and heat accumulation in the wall could not be ignored. In addition, the feed did not contain H_2O and CO_2 because they were presumed to be removed at a guard bed. Therefore, the feed-end temperature was only affected by heats of adsorption and desorption in PVSA operation. Therefore, another energy balance for the wall of the adsorption bed was introduced as follows:

$$A_w\rho_w C_{pw}\frac{\partial T_w}{\partial t}=2\pi R_{Bi}H_{in}(T-T_w)-2\pi R_{B0}H_{out}(T_w-T_{atm}) \quad (7)$$

Here, $A_w=\pi(R^2_{B,out}=R^2_{B,in})$

The pressure drop along the bed was calculated by Ergun's equation

$$-\frac{\partial P}{\partial z}=150\frac{(1-\varepsilon)^2}{\varepsilon^2}\frac{\mu u}{d_s^2}+1.75\frac{(1-\varepsilon)}{\varepsilon}\frac{\rho g u^2}{d_s} \quad (8)$$

The boundary conditions of mass and energy balances are as follows.

Boundary conditions for feed pressurization and adsorption steps:

$$-D_z\frac{\partial y_i}{\partial z}\bigg|_{z=0}=u|_{z=0}(y_i|_{z=0}-y_i|_{z=0+}) \qquad \frac{\partial y_i}{\partial z}\bigg|_{z=L}=0 \quad (9)$$

Boundary conditions for depressurizing pressure equalization, pressurizing pressure equalization, and vacuum steps:

$$\frac{\partial y_i}{\partial z}\bigg|_{z=0}=0 \qquad \frac{\partial y_i}{\partial z}\bigg|_{z=L}=0 \quad (10)$$

Boundary condition for heat flow:

$$K_L\frac{\partial^2 T}{\partial z^2}\bigg|_{z=0}=-\rho_g C_{pg}u|_{z=0}(T|_{z=0}-T|_{z=0+}) \qquad \frac{\partial T}{\partial z}\bigg|_{z=L}=0 \quad (11)$$

The sorption rate into the adsorbent pellet was described by the following linear driving force (LDF) model with a single lumped mass transfer parameter, ω

$$\frac{\partial q_i}{\partial t}=\omega_i(q_i^*-q_i) \quad (12)$$

The multi-component adsorption equilibrium was predicted by the following loading ratio correlation (LRC) model:

$$q_i^*=\frac{q_{mi}B_iP_i^{1/n_i}}{1+\sum_{i=1}^{n}B_iP_i^{1/n_i}} \quad (13)$$

In conventional PSA or PVSA simulations, only one bed can be simulated under the assumption that all beds in the process are identical. However, in one of the case studies, the beds in the PVSA process were asymmetric because one bed was poorly packed. Therefore, each bed in the two-bed PVSA process was separately simulated and the dynamic behavior of the PVSA process with asymmetric beds could be simulated by an integration of the dynamic simulation of each bed. The isotherm data of nitrogen, oxygen and argon from our previous study were used in the current study [34].

Table 3. Adsorption isotherm parameters of each gas on zeolite LiX

		Temperature		
		293 K	303 K	313 K
Nitrogen	q_m [mol/kg]	1.188	1.160	1.113
	$b\times10^{-3}$ [kPa^{-1}]	8.800	7.068	6.231
	Δq [%]*	1.601	3.278	0.855
Oxygen	q_m [mol/kg]	0.983	0.963	0.939
	$b\times10^{-3}$ [kPa^{-1}]	1.262	1.163	1.078
	Δq [%]*	1.587	2.284	2.509
Argon	q_m [mol/kg]	0.486	0.449	0.421
	$b\times10^{-3}$ [kPa^{-1}]	2.394	2.270	2.160
	Δq [%]*	1.000	3.604	4.235

$$*\Delta q[\%]=\frac{100}{k}\sum_{j=1}^{k}\left|\frac{q_j^{exp}-q_j^{cal}}{q_j^{exp}}\right|$$

The sequence of adsorption on the zeolite LiX was nitrogen, oxygen and argon, but there was little difference in adsorption amount between oxygen and argon. The experimental data were well fit by the LRC model and the adsorption parameters of each component are presented in Table 3. The deviation of average percent amount adsorbed (Δq (%)) is

$$\Delta q[\%]=\frac{100}{k}\sum_{j=1}^{k}\left|\frac{q_j^{exp}-q_j^{cal}}{q_j^{exp}}\right| \quad (14)$$

RESULTS AND DISCUSSION

Dry air (N_2 : O_2 : Ar=79 : 20 : 1 mol%) was supplied to the adsorption bed at 2.3 atm of adsorption pressure and a feed flow rate of

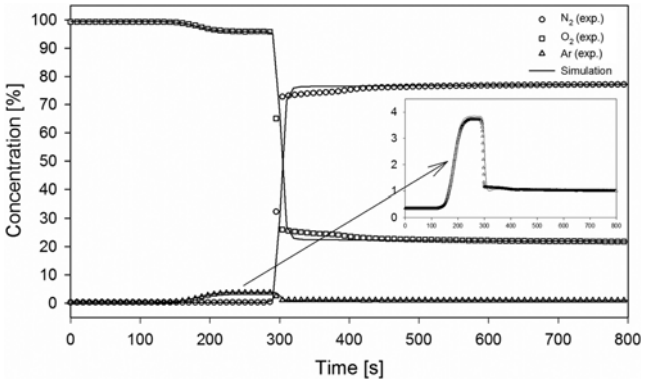

Fig. 3. Concentration breakthrough curves at the base condition in Table 2 (2.3 atm adsorption pressure and 4 LSTP/min flow rate).

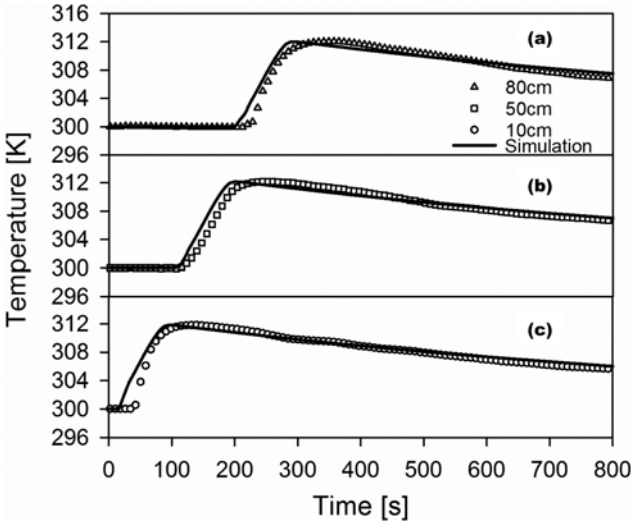

Fig. 4. Internal bed temperature profiles during breakthrough experiment at the reference condition in Table 2 (2.3 atm adsorption pressure and 4 LSTP/min flow rate): (a) 80 cm, (b) 50 cm and (c) 10 cm from the feed end of the bed.

4 LSTP/min. This was chosen as a reference condition in breakthrough and PVSA experiments as specified in Table 2. Then the effects of adsorption pressure and feed flow rate on adsorption dynamics were compared to the results at the reference condition.

1. Breakthrough Dynamics of the Zeolite LiX Bed

Fig. 3 shows the concentration profiles during the breakthrough experiment at the reference condition of 2.3 atm and 4 LSTP/min. The breakthrough of argon was observed near 150 s along with the simultaneous decrease of the oxygen concentration profile. The combined roll-up of O_2 and Ar was observed and its plateau was 3.7 mol%, which is almost four-times greater than the feed concentration. This roll-up phenomenon was due to the displacement of argon with nitrogen. Near 300 s, the breakthrough of nitrogen occurred and the concentration profiles of oxygen and argon were markedly decreased. In contrast, the concentration profile of nitrogen was increased up to the feed concentration (79%).

The temperature changes at the 0.1, 0.5 and 0.8 m locations from the feed end during the breakthrough experiment at the reference condition are presented in Fig. 4. The experimental temperature profiles agreed well with the predicted results regardless of the location along the column length. After a steep temperature excursion of 12 K, the temperature at each position decreased gradually due to heat loss through the column wall and cooling by the feed. Nevertheless, the temperature did not reach the initial temperature after 800 s. In Fig. 3, the breakthrough of argon and nitrogen occurred with an interval of 150 s. However, a single temperature excursion caused by the adsorption of nitrogen was observed in the temperature profile because of low concentration and weak adsorption of Ar on zeolite LiX. The maximum temperatures at 50 cm (middle of bed) and 80 cm (near product end) were observed at 200 s and 300 s, respectively.

2. Effect of Adsorption Pressure on Breakthrough Curve

Fig. 5 shows a comparison of breakthrough curves at 1.3, 2.3, 3.3 and 4.3 atm with a fixed feed flow rate of 4.0 LSTP/min. The breakthrough time was elongated with an increase in adsorption

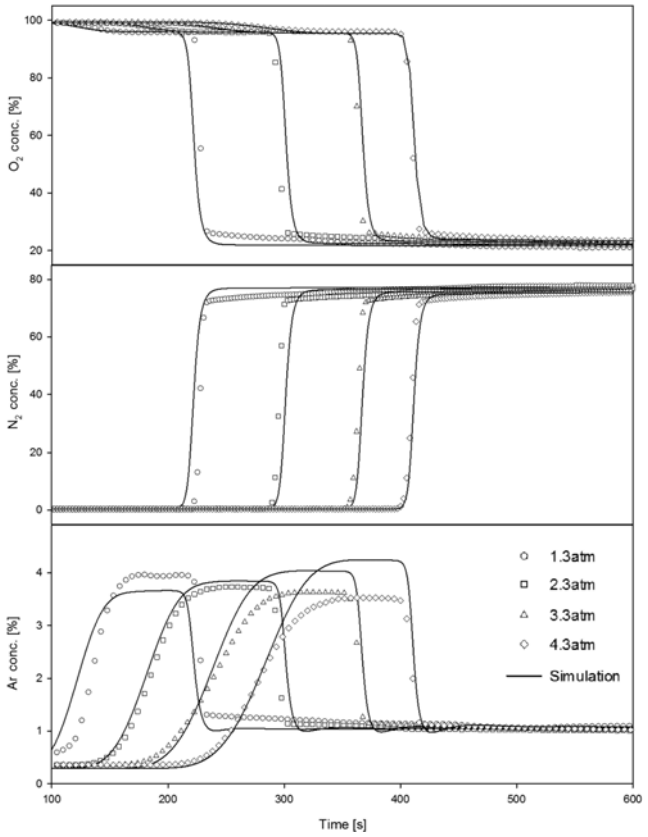

Fig. 5. Effect of adsorption pressure on breakthrough curves at a constant flow rate, 4 LSTP/min.

pressure because the adsorption capacity was increased with pressure. The breakthrough time of nitrogen at 1.3, 2.3, 3.3 and 4.3 atm was nearly 220, 300, 360 and 400 s, respectively, and the time gap between breakthrough curves decreased with increasing pressure.

The shape of the breakthrough curves for O_2 and N_2 seemed to be an almost constant pattern regardless of pressure. On the other hand, as the adsorption pressure increased, the height of Ar roll-up decreased a little, but the breakthrough curve of Ar became wider. The concentration wavefront of Ar was slightly affected by adsorption pressure, while the rear part of the breakthrough curve was mainly extended with an increase in pressure. The deviation of the simulated roll-up of Ar from the experimental result was observed in Fig. 5. Since the amount of Ar in the feed is 1 mol% (Ar partial pressure of 0.013-0.043 atm), the deviation seemed to come from the error of Ar isotherm in the low pressure range. However, due to small amount and weak adsorption of Ar, such deviation did not give any significant simulated deviation in the other components. The temperature profile for each breakthrough experiment is presented in Fig. 6. The temperature excursion at each position of the bed increased with pressure because of greater adsorption at higher pressure, and the temperature was increased up to 315 K (15 K increase) at 4.3 atm. The temperature excursion at the feed end (10 cm) was observed at a similar time regardless of adsorption pressure. Then, according to a propagation of the breakthrough curve, the propagation gap among temperature profiles at different pressure conditions was clearly observed near the product end (80 cm), and the propagation of the temperature profile was also elongated non-

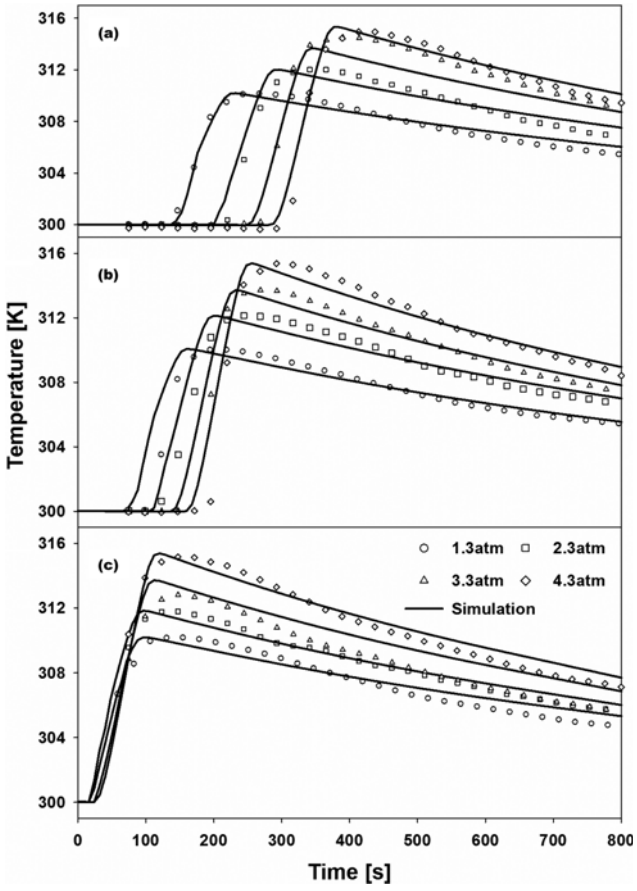

Fig. 6. Effect of adsorption pressure on the internal bed temperature profiles at constant flow rate, 4 LSTP/min: (a) 80 cm, (b) 50 cm and (c) 10 cm from the feed end of the bed.

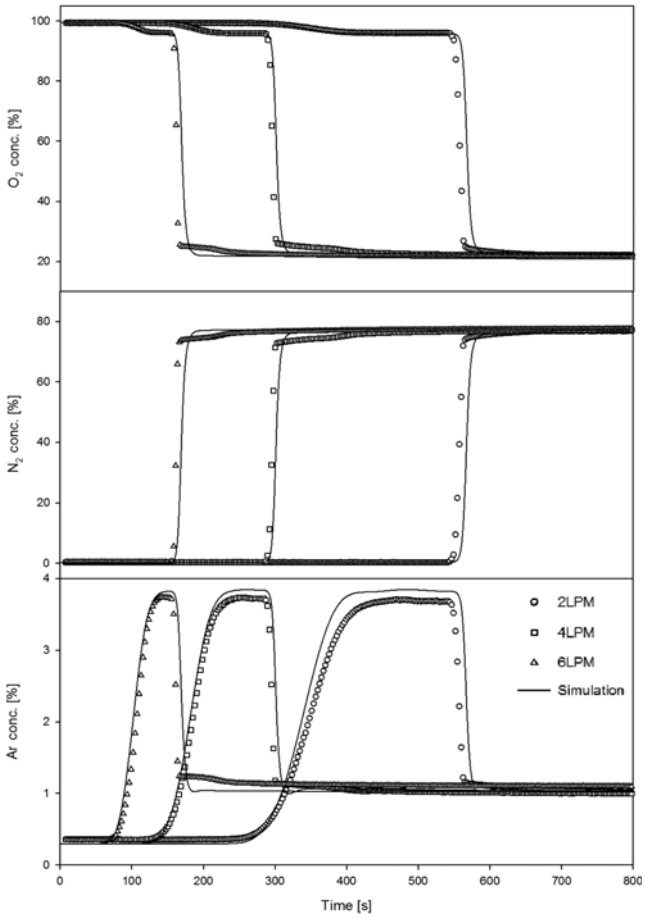

Fig. 7. Effect of feed flow rate on breakthrough curves at a constant adsorption pressure of 2.3 atm.

linearly. In addition, the wavefront of the temperature profile was almost constant, like the breakthrough curves of N_2 and O_2 in Fig. 5. On the other hand, the higher temperature excursion with pressure could contribute to a wider breakthrough curve of Ar.

3. Effect of Feed Flow Rate on Breakthrough Curve

Breakthrough curves at various feed flow rates under 2.3 atm are shown in Fig. 7. The breakthrough time decreased as the feed flow rate increased. The breakthrough curves of O_2 and N_2 maintained an almost constant pattern with respect to flow rate change, like the pressure results in Fig. 5. The breakthrough time of nitrogen was 160 s at 6 LPM, 300 s at 4 LPM, and 550 s at 2 LPM. Without any significant difference in maximum concentration of Ar, the breakthrough curve of Ar was narrower and its slope became steeper with an increase in flow rate.

Fig. 8 shows the temperature profiles during breakthrough at various flow rate conditions. The variation of temperature profiles was nonlinearly proportional to the change of flow rate, similar to the other results shown in Figs. 5-7. A gap among the temperature profiles was observed even at the feed end (10 cm), and increased with the propagation of the mass transfer zone, which is different from the pressure results in Fig. 6. The temperature excursion at 6 LSTP/min was higher than that at the other flow rate conditions, but the temperature decrease at this condition was faster than the others.

As mentioned previously, the temperature could have decreased due to heat loss through the column wall, as well as by convective heat transfer. The contribution of convective heat transfer to heat loss might be increased at elevated flow rate conditions. In addition, a high flow rate accompanied the short contact time between adsorbate and adsorbent. The non-linear variation of profiles by different flow rates means that a certain amount of time is required to overcome the mass transfer resistance. Such mass and heat transfer at high flow rate conditions led to an early breakthrough of N_2 and a narrow roll-up of Ar as shown in Fig. 7.

4. Fluid Dynamics of a Poorly Packed Bed in the PVSA Process

The pressure and flow patterns in the bed during the PVSA process were calculated using FLUENT. In the study, an unbalanced bed designed with tetrahedral mesh for a 3-dimensional bed was assumed to have additional voids at the feed inlet section, which stemmed from poor packing of the adsorbents. As mentioned before, the size of both beds was identical except for 1% void volume difference in the section from the feed inlet to 10 cm of one bed. However, the additional voids were negligible compared to the whole bed void (less than 0.05% difference).

The additional voids were negligible compared to the whole bed void, but generated a 1% void difference in the section from the feed inlet to 10 cm of the bed. All the steps in the PVSA process were simulated, but only the pressure and velocity distribution at

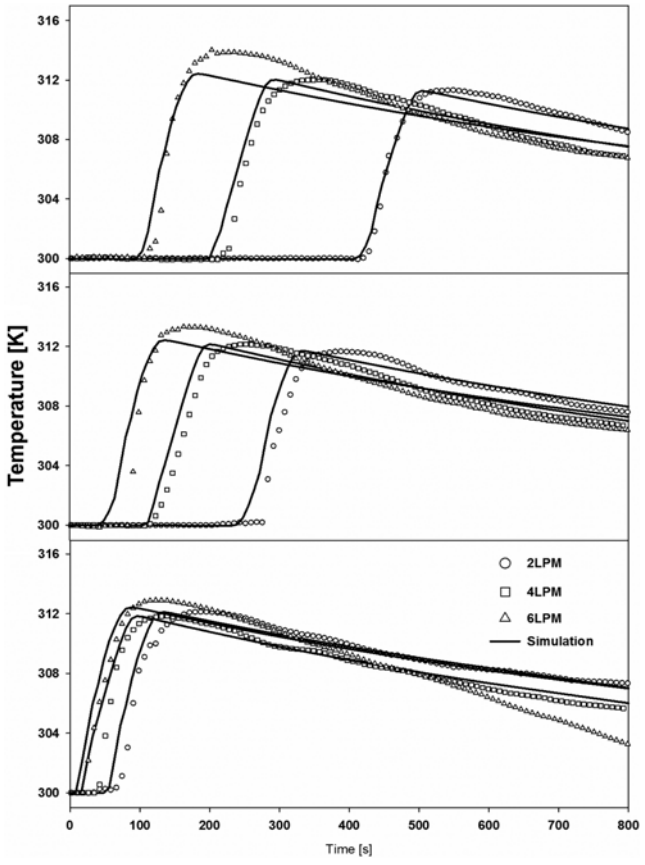

Fig. 8. Effect of feed flow rate on internal bed temperature profiles at each position: (a) 80 cm, (b) 50 cm, and (c) 10 cm from the feed end of the bed at a constant adsorption pressure of 2.3 atm.

the beginning of PR and DPE steps as representative non-isobaric steps are presented in Figs. 9 and 10, respectively. In the PR step of the conventional bed in Fig. 9(b), a maximum pressure was observed in the bottleneck part (feed-inlet line), which had a small cross sectional area. Right after this line, the pressure decreased steeply due to sudden expansion. The pressure pattern in the DPE step was similar to that at the PR step, but was elongated more because the gas exited through the bed end during the DPE step. The pressure profile of the poorly packed bed at the PR step in Fig. 9(a) was not very different than that of the conventional bed. However, the pressure distribution of the poorly packed bed in the DPE step was clearly worse than that of the conventional bed.

The corresponding velocity profiles for data in Fig. 9 are shown in Fig. 10. In both the PR and DPE steps, the velocity profile in the poorly packed bed was shorter than that in the conventional bed because the additional void led to a rapid change of velocity. Even though the overall pressure and temperature patterns between the two beds were almost the same in the simulation, the abnormal distribution of pressure and flow could have resulted in decreased adsorption efficiency in the poorly packed part of the bed. The bed inefficiency led to a decrease of the performance of the PVSA process.

5. Comparison of PVSA with One Poorly Packed Bed with Conventional PVSA

The PVSA process was tested under 2.3 atm adsorption pressure, 0.38 atm vacuum pressure and 4 LSTP/min flow rate. As mentioned before, the size of both beds was identical, but an additional 1% void volume by adding small pipe pieces was different in the section from the feed inlet to 10 cm of the bed.

Fig. 11(a) shows a cyclic temperature profile at a position of 10 cm from the feed inlet. The cyclic temperature profile gradually decreased up to the 10th cycle and then remained nearly constant.

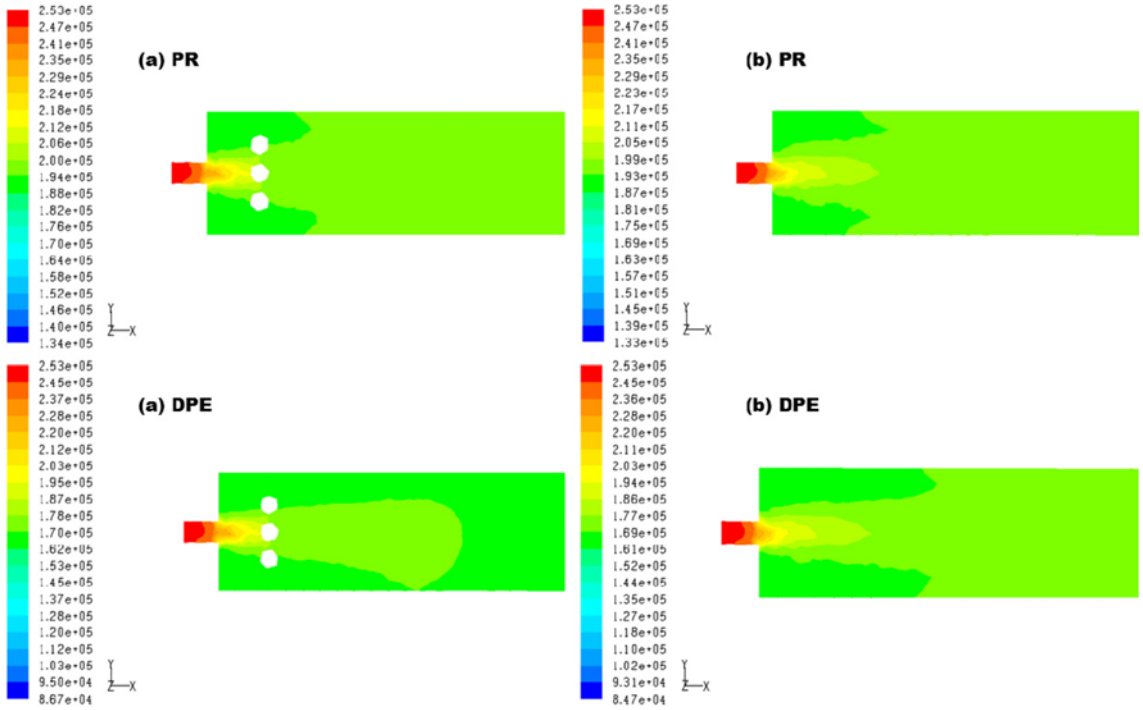

Fig. 9. Pressure profiles of (a) adsorption for the poorly packed bed in the feed-inlet section and (b) conventional bed at the beginning of the PR and DPE steps in PVSA process (y axis unit: Pa).

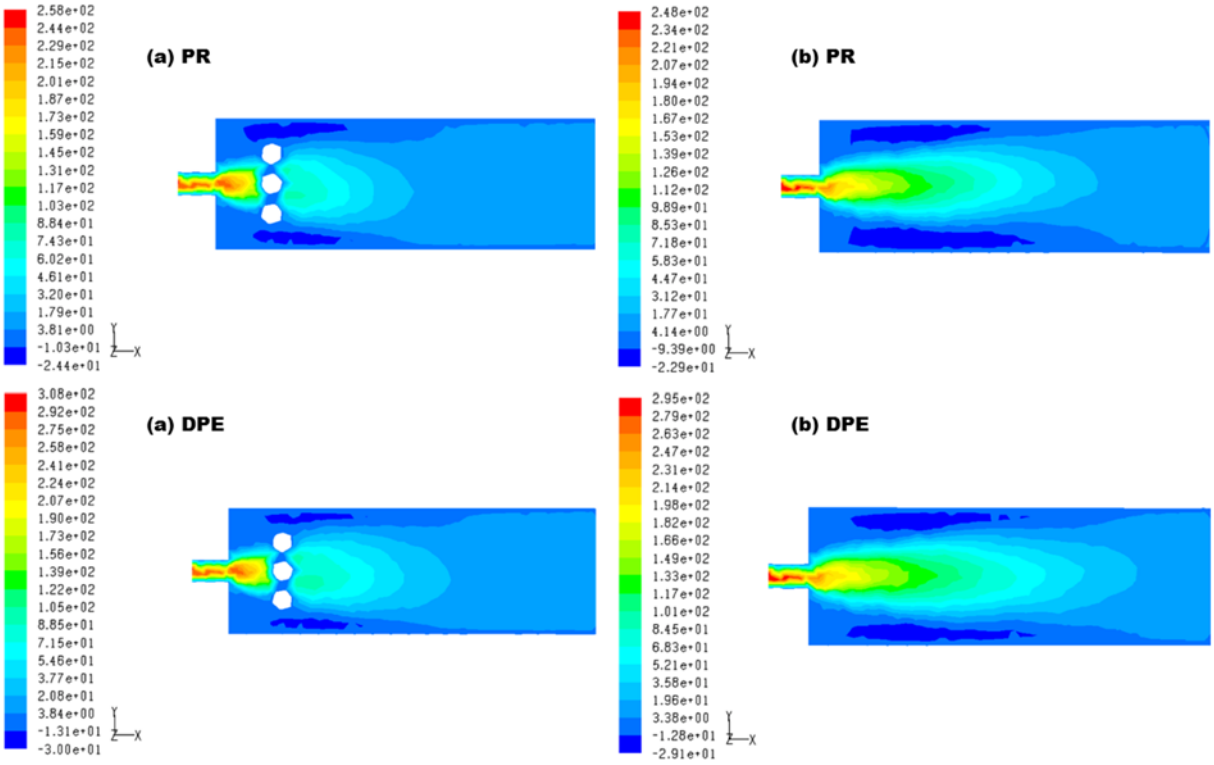

Fig. 10. Velocity profiles of (a) adsorption for the poorly packed bed in the feed-inlet section and (b) conventional bed at the beginning of the PR and DPE steps in the PVSA process (y axis unit: m/s).

The cyclic experimental temperature reached steady state at the 16th cycle as shown in Fig. 11(a). The increase in temperature occurred mainly at the pressurization step and, after a temperature decrease at the VU step, the bed temperature approached that at the PR step because of the adsorption that took place at the PPE step.

The average product purity of each PVSA cycle is presented in Fig. 11(b). Since the beds were initially filled with pure oxygen, the oxygen purity decreased with each cycle. After the 16th cycle, the purity changed slightly. Then, a steady state appeared to be reached by the 18th cycle, at which the experimental oxygen purity was 92.3 mol%. The experimental temperature had not dropped sufficiently compared to the simulated result in Fig. 11(a). This implied that a lower amount of adsorbate was desorbed during the desorption step so that the experimental purity was less than the simulated value. As shown in Fig. 11(b), the purity of PVSA with one poorly packed bed was almost 1% lower than that of conventional PVSA.

Bed imbalance can also stem from asymmetric piping because it leads to different flow rates at each bed. However, the experimental system in the study consisting of almost the same pipe length was applied to each bed, and the pressure drop difference between two beds was negligible compared to the conventional PVSA run. The performance difference in Fig. 11(b) may stem from the difference in adsorbent amount because the same size of beds was applied to both PVSA runs. Main difference is an additional 1% void volume in the section from the feed inlet to 10 cm of the bed. However, the additional void volume caused by poor packing at the feed end in one bed was less than 0.05% of the total bed volume. Therefore, it was expected that the performance decrease mainly came from the distribution of flow and pressure in the poorly packed bed at the initial period of step time. This small asymmetry in bed end between two beds led to a performance decrease in the cyclic process.

CONCLUSION

The five-step two-bed PVSA process using zeolite LiX for air separation was studied both experimentally and theoretically. The effect of the adsorption pressure and flow rate on the adsorption dynamics of a zeolite LiX bed was studied via breakthrough experiments using air (78 mol% N_2, 21 mol% O_2 and 1 mol% Ar).

The variations in the breakthrough curves were not linearly proportional to variations of adsorption pressure and flow rate. A higher adsorption pressure and feed flow rate led to a greater temperature increase in the bed. The effect of adsorption pressure on bed temperature variation was greater than that of the feed flow rate. While the breakthrough curves of O_2 and N_2 showed a nearly constant pattern regardless of adsorption pressure and flow rate, the concentration profile of Ar was affected by the breakthrough conditions due to competitive adsorption with N_2 and heat transfer. And the plateau of Ar and O_2 roll-up by N_2 propagation reached almost the concentration of 4 mol%. However, the effect of Ar adsorption on the breakthrough curve and bed temperature was negligible due to its low concentration and weak adsorption affinity.

The fluid dynamic behavior of the poorly packed bed was simulated at each step in the PVSA process. The distribution of pressure and velocity profile in the poorly packed bed became worse than that in a normal bed, especially at non-isobaric steps. From the viewpoint of bed utilization efficiency, even a small component of poor packing in the bed could result in a decrease of the separation effi-

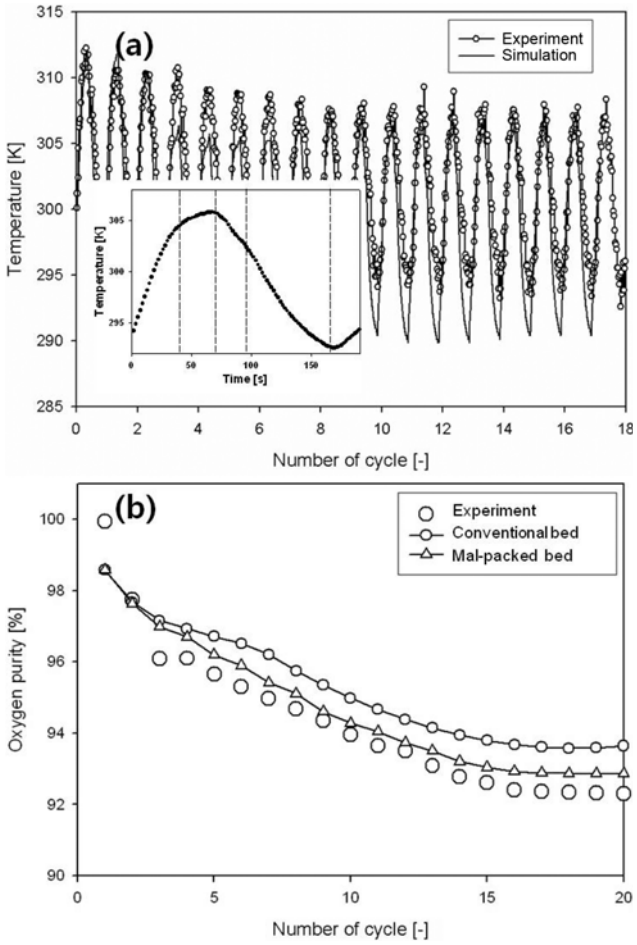

Fig. 11. Variation of (a) temperature and (b) product purity during the PVSA operation at 2.3 atm adsorption pressure and 4 LSTP/min flow rate.

ciency in the cyclic process, because it leads to changing flow rate and pressure distribution at the initial stage of each step. Therefore, small asymmetries due to poor packing between beds could greatly reduce the product purity in the PVSA process.

ACKNOWLEDGEMENTS

This work was supported by the Korean Institute of Energy Technology Evaluation and Planning (KETEP) and Ministry of Knowledge Economy (MKE) (2011-8510020030).

LIST OF SYMBOLS

A : cross-sectional area [cm^2]
B : Langmuir isotherm parameter [kPa^{-1}]
C : concentration [mole/L]
C_p : heat capacity [J/g K]
d : diameter [cm]
D_{ax} : mass axial dispersion coefficient [cm^2/s]
h : heat transfer coefficient [J/cm^2 s K]
$-\Delta H$: average heat of adsorption [J/mole]
K_z : effective axial thermal conductivity [J/cm s K]
L : bed length [cm]
P : pressure [Pa]
q, q*, $\bar{q}$: amount adsorbed, equilibrium amount adsorbed, and average amount adsorbed, respectively [mol/g]
q_m : Langmuir isotherm parameter [mol/g]
R : radius, cm, or gas constant [J/mol·K]
t : time [s]
T : solid phase and gas phase temperature [K]
T_{atm} : ambient temperature [K]
T_w : wall temperature [K]
u : interstitial velocity [cm/s]
y : mole fraction in gas phase
z : axial position in an adsorption bed [cm]

Greek Letters

ε : interparticle void fraction
μ : viscosity [cm/g·s]
ν : superficial velocity [cm/s]
ρ : density [cm^3/g]
ω : LDF coefficient [s^{-1}]

Subscripts

B : bed
i : component i, inner bed
o : outer bed
p : pellet
g : gas phase
s : solid phase
w : wall

REFERENCES

1. X. Shuai, S. Cheng and A. Meisen, *Micropor. Mater.*, **5**, 347 (1996).
2. J. C. Santos, P. Cruz, T. Regala, F. D. Magalhães and A. Mendes, *Ind. Eng. Chem. Res.*, **46**, 591 (2006).
3. S.-J. Lee, J.-H. Jung, J.-H. Moon, J.-G. Jee and C.-H. Lee, *Ind. Eng. Chem. Res.*, **46**, 3720 (2007).
4. A. Jayaraman, R. Yang, S.-H. Cho, T. G. Bhat and V. Choudary, *Adsorption*, **8**, 271 (2002).
5. J.-G. Jee, M.-B. Kim and C.-H. Lee, *Chem. Eng. Sci.*, **60**, 869 (2005).
6. Y. Y. Li, S. P. Perera and B. D. Crittenden, *Chem. Eng. Res. Des.*, **76**, 921 (1998).
7. R. Kumar, *Sep. Sci. Technol.*, **31**, 877 (1996).
8. S. Sircar, *Ind. Eng. Chem. Res.*, **41**, 1389 (2002).
9. A. Mivechian and M. Pakizeh, *Korean J. Chem. Eng.*, **30**, 937 (2013).
10. T. J. Giesy and M. D. LeVan, *Chem. Eng. Sci.*, **90**, 250 (2013).
11. J.-G. Jee, S.-J. Lee, M.-B. Kim and C.-H. Lee, *AIChE J.*, **51**, 2988 (2005).
12. R. Arvind, S. Farooq and D. M. Ruthven, *Chem. Eng. Sci.*, **57**, 419 (2002).
13. J.-G. Jee, S.-J. Lee and C.-H. Lee, *Korean J. Chem. Eng.*, **21**, 1183 (2004).
14. R. S. Todd and P. A. Webley, *AIChE J.*, **52**, 3126 (2006).
15. A. Nakhaeipour and A. Nakhaeipour, *Chem. Eng. Tehcnol.*, **29**, 50 (2006).
16. S. Farooq, D. M. Ruthven and H. A. Boniface, *Chem. Eng. Sci.*, **44**, 2809 (1989).

17. G. Reiβ, *Gas Sep. Purif.*, **8**, 95 (1994).
18. M. Kawai and T. Kaneko, *Gas Sep. Purif.*, **3**, 2 (1989).
19. S. J. Wilson and P. A. Webley, *Ind. Eng. Chem. Res.*, **41**, 2753 (2002).
20. L. Jiang, L. T. Biegler and V. G. Fox, *AIChE J.*, **49**, 1140 (2003).
21. A. M. M. Mendes, C. A. V. Costa and A. R. E. Rodrigues, *Sep. Purif. Technol.*, **24**, 173 (2001).
22. T. R. Gaffney, *Curr. Opin. Solid State Mater. Sci.*, **1**, 69 (1996).
23. S. Natarajan, C. Zhang and C. Briens, *Powder Technol.*, **152**, 31 (2005).
24. M. Nijemeisland and A. G. Dixon, *Chem. Eng. J.*, **82**, 231 (2001).
25. M. Coussirat, A. Guardo, B. Mateos and E. Egusquiza, *Chem. Eng. Sci.*, **62**, 6897 (2007).
26. A. Guardo, M. Coussirat, F. Recasens, M. A. Larrayoz and X. Escaler, *Chem. Eng. Sci.*, **62**, 5503 (2007).
27. S. A. Nouh, K. K. Lau and A. M. Shariff, *J. Appl. Sci.*, **10**, 3229 (2010).
28. M. Rahimi and M. Mohseni, *Korean J. Chem. Eng.*, **25**, 395 (2008).
29. M. W. Ackley and J. Smolarek, U.S. Patent, 6,790,260 B2 (2004).
30. Q. Huang and M. Eić, *Sep. Purif. Technol.*, **103**, 203 (2013).
31. C.-H. Lee, J. Yang and H. Ahn, *AIChE J.*, **45**, 535 (1999).
32. C. C. K. Beh and P. A. Webley, *Adsorption Sci. Technol.*, **21**, 319 (2003).
33. Y. Lü, S.-J. Doong and M. Bülow, *Adsorption*, **9**, 337 (2003).
34. Y.-J. Park, S.-J. Lee, J.-H. Moon, D.-K. Choi and C.-H. Lee, *J. Chem. Eng. Data*, **51**, 1001 (2006).